Biases in parameter estimation from overlapping gravitational-wave signals in the third-generation detector era

Anuradha Samajdar[1,2,3] Justin Janquart[1,2] Chris Van Den Broeck,[1,2] and Tim Dietrich[4,5]

[1]*Nikhef, Science Park 105, 1098 XG Amsterdam, Netherlands*
[2]*Institute for Gravitational and Subatomic Physics (GRASP), Utrecht University,*
Princetonplein 1, 3584 CC Utrecht, Netherlands
[3]*Department of Physics, University of Milano–Bicocca, Piazza della Scienza 3, 20126 Milano, Italy*
[4]*Institut für Physik und Astronomie, Universität Potsdam, Haus 28,*
Karl-Liebknecht-Strasse 24/25, 14476 Potsdam, Germany
[5]*Max Planck Institute for Gravitational Physics (Albert Einstein Institute), Am Mühlenberg 1,*
Potsdam 14476, Germany

In the past few years, the detection of gravitational waves from compact binary coalescences with the Advanced LIGO and Advanced Virgo detectors has become routine. Future observatories will detect even larger numbers of gravitational-wave signals, which will also spend a longer time in the detectors' sensitive band. This will eventually lead to overlapping signals, especially in the case of Einstein Telescope (ET) and Cosmic Explorer (CE). Using realistic distributions for the merger rate as a function of redshift as well as for component masses in binary neutron star and binary black hole coalescences, we map out how often signal overlaps of various types will occur in an ET-CE network over the course of a year. We find that a binary neutron star signal will typically have tens of overlapping binary black hole and binary neutron star signals. Moreover, it will happen up to tens of thousands of times per year that two signals will have their end times within seconds of each other. In order to understand to what extent this would lead to measurement biases with current parameter estimation methodology, we perform injection studies with overlapping signals from binary black hole and/or binary neutron star coalescences. Varying the signal-to-noise ratios, the durations of overlap, and the kinds of overlapping signals, we find that in most scenarios the intrinsic parameters can be recovered with negligible bias. However, we find large offsets for a short binary black hole or a quieter binary neutron star signal overlapping with a long and louder binary neutron star event when the merger times are sufficiently close. Although based on a limited number of simulations, our studies may be an indicator of where improvements are required to ensure reliable estimation of source parameters for all detected compact binary signals as we go from second-generation to third-generation detectors.

I. INTRODUCTION

The direct observation of gravitational waves (GWs) [1] has had a tremendous impact in fundamental physics [2–5], astrophysics [6–15], and cosmology [16–18] and, starting from the observation of the binary neutron star (BNS) signal GW170817 [9], has opened a new era in multi-messenger astronomy with GWs [19–22]. The third observing run (O3) of Advanced LIGO [23] and Advanced Virgo [24] ended in March 2020, and together these interferometers have found more than 50 GW candidates [25], with 39 candidates observed during the first half of O3 [8]. The detector sensitivities will be improved further, and the frequency with which signals are observed is expected to keep increasing in coming years. In particular, in the transition to the envisaged third-generation (3G) era, with Einstein Telescope (ET) [26,27] and Cosmic Explorer (CE) [28–30], the detection rate will go up steeply, and signals will also spend much longer times in the detectors' sensitive band [31]. As first pointed out in Ref. [32] and studied further in this paper, the probability of overlapping signals will then become significant.

In view of this, it will be important to assess to what extent the science goals of 3G detectors (see, e.g., [31,33–42]) may be affected by signals overlapping with each other. Apart from science with signals from compact binary coalescences (CBCs), this includes searches for primordial backgrounds, since the subtraction of "foreground" CBC sources [30,43–47] will rely on our ability to characterize them individually. As shown in Refs. [48,49], even using current data analysis techniques, the *detection rates* of individual CBC sources would likely not be significantly impacted by the occurrence

of overlapping signals. However, a study of the effect on *parameter estimation* had not yet been performed.[1]

Earlier works [52–54] have studied parameter estimation for single sources in the 3G era. Here we take the first step in assessing possible biases in the recovery of parameters characterizing a GW signal when signals from different sources are simultaneously present in the detectors' sensitive band. Before doing this, we map out how often signal overlaps of various types will occur in a network of two CEs and one ET over the course of a year, assuming realistic distributions for merger rate as a function of redshift and for component masses in binary neutron star and binary black hole (BBH) coalescences. We find that a typical BNS signal will be overlapped by tens of BBH signals. Moreover, BBH or BNS signals whose mergers occur within seconds from each other will be quite common. Since these are the cases for which we can expect the largest parameter estimation biases to occur, we focus on them in setting up simulations whereby signals are added to synthetic data from the ET-CE network and analyzed using current state-of-the-art parameter estimation techniques. We explore various scenarios of signals from different kinds of sources overlapping: two BBH signals, two BNS signals, and a BBH signal with a BNS. For our simulations, we choose signal parameters consistent with what has been observed as being representative of each kind of source: parameter values similar to the ones of GW170817 [55] to represent a BNS, similar to the ones of GW150914 [56] to represent a high-mass BBH, and similar to the ones of GW151226 [57] for a lower-mass BBH. We find that, in most cases, the intrinsic parameters can be recovered with negligible bias. However, if the merger times of the two signals are sufficiently close, considerable biases can occur when a short BBH signal or a quieter BNS signal overlaps with a louder BNS signal. Though our study should be considered exploratory, it already points to where improvements over current parameter estimation pipelines will be needed the most.

This paper is structured as follows. In Sec. II, we obtain detection rate estimates for signals in the 3G era, from which we calculate overlap rates. In Sec. III, we lay out the settings and methods we use for parameter estimation. Parameter estimation results for various scenarios are shown in Sec. IV. A summary and conclusions are presented in Sec. V, where we also give recommendations for future improvements of parameter estimation techniques.

II. OVERLAP RATE ESTIMATES

A. Methodology

Before looking at the impact of overlapping signals on parameter estimation for the individual ones, we want to

address the question of how frequently such overlaps will occur, depending on the type. Previous characterizations of the overlap probabilities for 3G detectors were based on the *duty cycle*, which is defined as the ratio of the typical duration of a particular type of event (BNS or BBH) to the average time interval between two successive events of that type, assuming some fixed canonical values of the component masses for each type [32]. However, here we also want to allow for overlaps of mixed types and for a range of component masses (and, hence, signal durations) within a given type, so as to arrive at a detailed assessment of overlap rates. Therefore, what we will do is to assume particular merger rates as a function of the redshift for BBH and BNS, as well as component mass distributions, and on the basis of these create simulated "catalogs" of signals in the detectors. This will allow us to make quantitative statements regarding BNS signals overlapping with other BNS signals and with BBHs, and the same for overlaps of BBH with BBH events, in a much more detailed and realistic fashion.[2]

We start by estimating the number of individual BBH and BNS coalescences that happen in a given volume, up to a maximum redshift which is chosen to be $z_{max} = 30$ for BBH events and $z_{max} = 6$ for BNS events [31,32,48,59]. For this, we need the intrinsic merger rate density for the events as a function of the redshift. We will assume that the compact binaries originate from stellar populations and adopt the merger rate estimates of Belczynski *et al.* [60] with Oguri's analytical fit [61],[3] whose general expression is

$$R_{GW}(z) = \frac{a_1 e^{a_2 z}}{e^{a_3 z} + a_4} \ \text{Gpc}^{-3} \ \text{yr}^{-1}. \tag{1}$$

The coefficients a_i, $i = 1, \ldots, 4$, depend on the star populations that are considered; see Fig. 1. For our purposes, we consider the combination of population I and II stars for BNS, and populations I, II, and III for BBH, as the contribution of the latter type of stars is important only at redshifts of $\gtrsim 4$. However, these relations are rescaled to match the local merger rate estimates obtained observationally by LIGO and Virgo so far; see [62]. In this work, we focus on the lowest, the median, and the highest local rate for each type of event. For BNS, the lowest, median, and highest local rates are, respectively, 80, 320, and 810 $\text{Gpc}^{-3} \text{yr}^{-1}$, which are obtained by changing the value of a_1 to 2480, 9920, and

---

[1]Around the time of publication, Ref. [50] performed parameter estimation studies on overlapping systems and Ref. [51] suggested ways to correct biases from presence of overlapping signals.

[2]Since neutron star–black hole (NS-BH) rates are less certain (see, e.g., [13,58]), we will not consider them here, but we expect general conclusions regarding parameter estimation to largely carry over when signal durations are similar.

[3]Strictly speaking, this merger rate distribution refers to BBH mergers. However, when computing the merger rate density (see, e.g., [48,59,60]), one assumes a time delay distribution [e.g., $P(t_d) \propto 1/t_d$], with a minimum time delay that is higher for BBH than for BNS. Using the distribution of Ref. [60] for both BNS and BBH (with some overall rescaling) then implies that we will underestimate the BNS merger rate density [59] and, hence, the frequency of overlaps involving BNS signals.
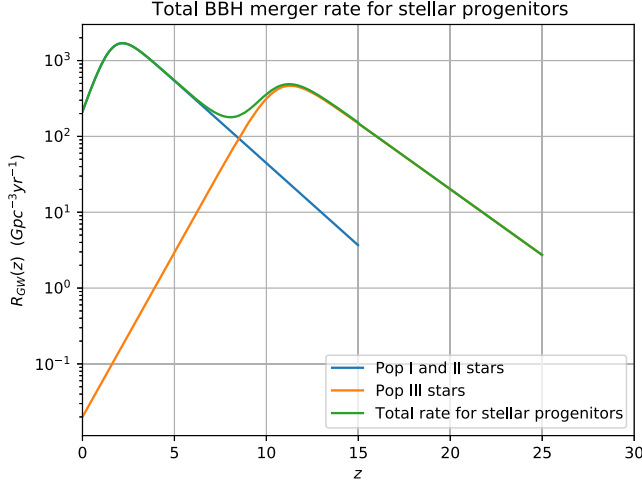
FIG. 1. The BBH merger rate density according to Oguri's fit [61] for population I, II, and III stars, as well as the total rate, when all the star populations are accounted for.

25110, respectively. On the other hand, for the BBH events, we apply a multiplicative constant to the sum of the population I and II and the population III rates, equal to 0.0709, 0.112, and 0.178 for the lowest, median, and highest local rates, which are 15.1, 23.8, and 37.9 Gpc^{-3} yr^{-1}, respectively.

An intrinsic merger rate density $R_{GW}(z)$ is then converted to an *observed* merger rate density as a function of the redshift by multiplying by the differential comoving volume [32]:

$$R_{GW}^{obs}(z) = R_{GW}(z)\frac{dV_c}{dz}(z). \qquad (2)$$

Note that the factor $(1 + z)$ needed to convert from time at the source to time at the observer is already included in $R_{GW}(z)$. To obtain dV_c/dz, we assume the *Planck13* cosmological model [63] of ASTROPY [64,65].

As a next step, we simulate the population of systems by constructing a "catalog" and determine which events are actually detected. For the BBH population, we assume that the masses follow the "*power law+peak*" distribution presented in Ref. [62] for the primary component mass and the corresponding power law distribution for the mass ratio, through which we sample the secondary mass [62]. For BNS events, we distribute component masses uniformly, where for the primary mass $m_1 \in [1, 2.5]$ $M_\odot$ and for the secondary mass $m_2 \in [1 M_\odot, m_1]$. Events are distributed over comoving distance D according to $R_{GW}(z)$, converting between D and z using the above-mentioned cosmology and cutting off at the maximum redshifts z_{max} stated above. Sky positions and unit normals to the orbital plane are taken to be uniform on the sphere.

Before continuing, we stress that, although for the purposes of this paper we expect both our merger rate

and mass distributions to be sufficiently indicative of the true distributions, in both cases they should be treated as approximate and subject to future updates (indeed, 3G detectors have the potential to measure them with far greater accuracy [38]).

In this work, we assume a network of two CEs located at the LIGO Hanford and Livingston sites and one ET located at the Virgo site. For each event, we calculate the optimal signal-to-noise ratios (SNRs) in the three observatories, which are added in quadrature to obtain a network SNR. In computing SNRs, we consider only the inspiral part of binary coalescence, so that in the stationary phase approximation [66] and for a single interferometer [67]

$$\text{SNR} = \frac{1}{2}\sqrt{\frac{5}{6}}\frac{1}{\pi^{2/3}}\frac{c}{D(1+z)^{1/6}}\left(\frac{G\mathcal{M}}{c^3}\right)^{5/6}$$
$$\times g(\theta, \phi, \psi, \iota)\sqrt{I(\mathcal{M})}. \qquad (3)$$

Here $\mathcal{M} = (m_1 m_2)^{3/5}/(m_1 + m_2)^{1/5}$ is the chirp mass in the source frame. The geometric factor is given by

$$g(\theta, \phi, \psi, \iota) = (F_+^2(\theta, \phi, \psi)(1 + \cos(\iota)^2)^2$$
$$+ 4F_\times^2(\theta, \phi, \psi)\cos(\iota)^2)^{1/2}, \qquad (4)$$

where $F_{+,\times}$ are the beam pattern functions in terms of sky position (θ, ϕ) and polarization angle ψ, while ι is the inclination angle. We take Einstein Telescope to consist of three detectors with 60° opening angle, arranged in a triangle with sides of 10 km [68], and add the corresponding SNRs in quadrature; for Cosmic Explorer, we assume a single L-shaped detector of 40 km arm length [28,29]. Finally,

$$I(\mathcal{M}) = \int_{f_{low}}^{f_{high}} \frac{f^{-7/3}}{S_h(f)} df. \qquad (5)$$

Here f_{low} is a low-frequency cutoff that depends on the observatory; we set $f_{low} = 5$ Hz for both ET and CE, though lower values may be achieved in the case of ET [69,70]. For f_{high}, we use the frequency of the innermost stable circular orbit:

$$f_{high}(m_1, m_2, z) = \frac{1}{1+z}\frac{1}{6\pi\sqrt{6}}\frac{c^3}{GM}, \qquad (6)$$

where $M = m_1 + m_2$ is the total mass. We take the noise power spectral density (PSD) $S_h(f)$ to be ET-D in the case of Einstein Telescope [26,27]; for the projected PSD of Cosmic Explorer, see [28,29].[4]

---

[4]For a discussion of issues related to computing PSDs in the presence of overlapping signals, and possible solutions, see Secs. III and V.

TABLE I. The number of events detected by a network of two CEs and one ET in a particular realization of one year of data, the median network SNRs and their 90% spreads, and the detection numbers and percentages (in parentheses) for different choices of minimum network SNR.

	No. of detections	SNR_{net}	No. with $SNR_{net} > 250$	No. with $SNR_{net} > 100$	No. with $SNR_{net} > 50$	No. with $SNR_{net} > 20$
BBH						
Low rate	53756	$81.1^{+94.2}_{-57.3}$	3069 (5%)	20605 (35%)	40063 (68%)	52239 (89%)
Median rate	85725	$81.3^{+93.9}_{-57.5}$	4972 (5%)	33148 (39%)	63958 (75%)	83333 (97%)
High rate	137225	$81.5^{+94.2}_{-57.4}$	7860 (6%)	53419 (39%)	102766 (75%)	133460 (97%)
BNS						
Low rate	98898	$19.2^{+22.1}_{-4.9}$	17 (0.017%)	298 (0.30%)	2712 (2.7%)	44350 (48%)
Median rate	396793	$19.1^{+22.0}_{-4.8}$	73 (0.018%)	1257 (0.32%)	10659 (2.7%)	177296 (45%)
High rate	1004525	$19.1^{+22.1}_{-4.8}$	196 (0.020%)	3255 (0.32%)	27135 (2.7%)	448610 (45%)

The network SNR, denoted SNR_{net}, is defined as

$$SNR^2_{net} = \sum_{i=1}^{3} SNR^2_i, \tag{7}$$

where the sum is over the two CE and the one (triangular) ET observatories. We consider an event as detectable if the network SNR is above 13.85 ($= \sqrt{3} \times 8$), without imposing SNR thresholds in individual observatories. For the BNS and BBH mass ranges considered here, this means that detection rates will mainly be driven by the CEs, but we note that ET will have an advantage at higher masses [71].

Finally, signals will be present in a detector for a duration given by

$$\tau = 2.18 \left(\frac{1.21 \, M_\odot}{(1+z)\mathcal{M}}\right)^{5/3}$$
$$\times \left[\left(\frac{100 \, \text{Hz}}{f_{low}}\right)^{8/3} - \left(\frac{100 \, \text{Hz}}{f_{high}}\right)^{8/3}\right] \text{s.} \tag{8}$$

Simulated catalogs of events happening over the course of a year are constructed as follows. The year is split into a grid in which each cell corresponds to one second, and merger times are drawn from a uniform distribution over these cells. For a given type of event (BNS or BBH), one associates to each merger time a mass pair, redshift, sky position, and orientation of the orbital plane drawn from the corresponding distributions, as well as a signal duration computed from Eq. (8). Doing this for the three choices of local merger rate, and in each case putting together the BNSs and BBHs, catalogs of events are obtained. Finally, within each catalog, it is assessed which events will be detectable with the ET-CE network according to the criteria spelled out above, leading to an overview of what we may expect to be contained in one year's worth of data. In particular, we can check how often and in what way events tend to overlap, depending on their types.

B. Overlap estimates

The three different local merger rates give the following typical numbers of events happening over one year, prior to imposing detectability thresholds: ~59000, 93000, and 148000 BBH events and 286000, 1145000, and 2900000 BNS events for the low, median, and high local rate, respectively. The network of two CEs and one ET will detect 93% of BBHs and 35% of BNSs. The number of detected signals is shown in Table I for the three local rates, along with median and 90% spreads on SNRs, and a breakdown of detections according to their loudness. In Fig. 2, we also show the normalized SNR distributions for BNS and BBH, compared with the $1/SNR^4$ distribution one would have in a Euclidean universe with sources distributed uniformly in volume [72]. As expected,
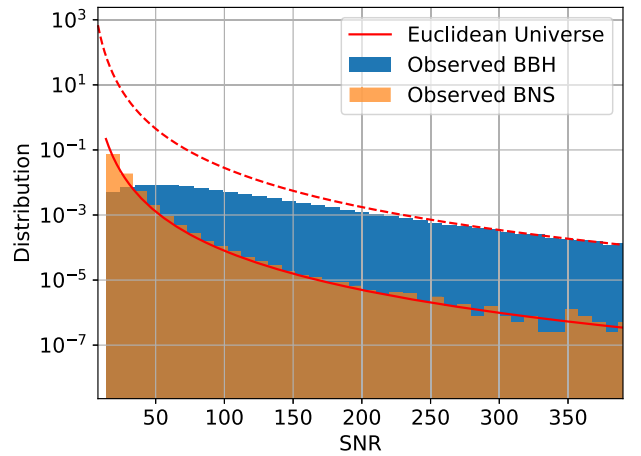

FIG. 2. Normalized distributions of SNRs for BNSs (orange histogram) and BBHs (blue histogram) and for illustrative purposes the $1/SNR^4$ distribution one would have in a Euclidean universe with sources placed uniformly in volume (red solid curve for BNSs; red dashed, non-normalized curve for BBHs). BBHs can be seen out to redshifts where cosmological effects are important, causing the $1/SNR^4$ curve to deviate from the true distribution at low SNR.

TABLE II. The number of seconds in a year with at least two mergers occurring, depending on their types.

Rate	BBH mergers > 1	BNS mergers > 1	Any mergers > 1
Low rate	48	155	374
Median rate	127	2412	3663
High rate	303	15581	20149

BBHs do not follow the latter distribution at low SNR, because they can be seen out to redshifts where cosmological effects have a crucial impact, but BNS events are fairly consistent with it.

Within our simulated catalogs of events, we can look at the numbers of detected signals that overlap depending on the types. We focus on two quantities: (i) the number of seconds in a year where at least two detected signals have their merger and (ii) the typical number of mergers that happen during the time a given signal is in a detector's sensitivity band.

The numbers of seconds in a year that have at least two mergers taking place is given in Table II; clearly, this will happen frequently over the course of a year. Indeed, we find that even more than two mergers can occur within the same second. The proportion of detected signals merging together with at least one other goes up with increasing local merger rate, potentially reaching thousands per year.

In addition to the scenario where different compact binary mergers happen in the same second, we investigate the typical number of mergers that will happen over the entire duration of a BNS event while it is in the band, depending on their type; see Table III and Fig. 3. Because BNS events are in the detector band for a long time (several hours for $f_{\rm low} = 5$ Hz), quite a number of such overlaps will indeed occur. If one does the same for BBHs, one finds that either zero or one BBH or BNS merger (at 90% confidence) will happen in its duration; this is due to BBH events being shorter (the median duration being ~ 45 s).

Before moving on to parameter estimation issues, let us briefly look at other future GW observatories that are being planned or considered. Constructing simulated catalogs of detectable sources in the same way as above and focusing on the high local merger rate, we find that, over the course of a year, Advanced LIGO+ [73] will typically have no
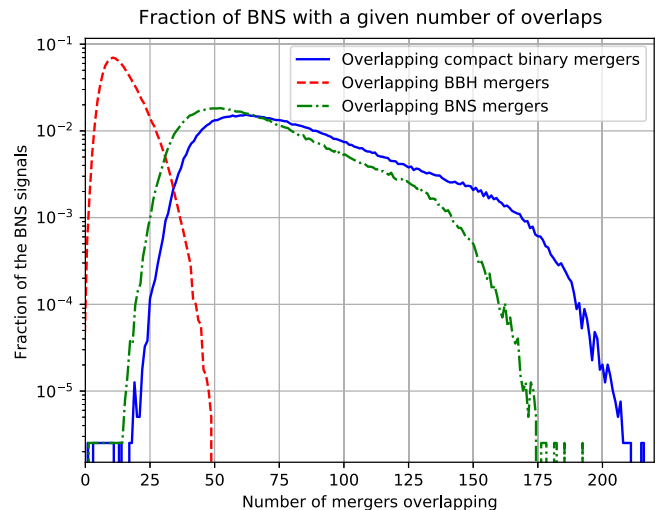

FIG. 3. Fraction of detected BNS mergers with a given number of compact binary mergers (blue curve), BBH mergers (red curve), and BNS mergers (green curve) taking place while the BNS signal is in the band.

events merging within the same second and only a few occurrences of a BBH merging in the duration of a BNS (assuming $f_{\rm low} = 15$ Hz). For *Voyager* [74], we find $\mathcal{O}(1)$ instances of two events merging within the same second, and BNS signals will typically have at most one other signal's merger in their duration (for $f_{\rm low} = 10$ Hz). These numbers refer to signals detectable with a single interferometer (with SNR threshold 8) rather than with a network of them, but it will be clear that overlapping signals are going to become an important consideration mainly in the 3G era.

III. PARAMETER ESTIMATION SETUP

Having established that third-generation detectors will see a considerable number of overlapping signals whose mergers occur very close in time, we want to find out what this will imply for parameter estimation. To this end, we simulate BBH and BNS signals in a network consisting of one ET and two CE observatories as in the previous section, assuming stationary, Gaussian noise following the PSDs used above.

Since we expect parameter estimation biases to be more pronounced when SNRs of overlapping signals are similar

TABLE III. Typical numbers of compact binary mergers happening during the time a BNS signal is in the band.

Rate	Number of BBH mergers	Number of BNS mergers	Number of any type
Low rate	8^{+10}_{-5}	16^{+16}_{-8}	25^{+23}_{-12}
Median rate	13^{+14}_{-7}	62^{+58}_{-27}	76^{+77}_{-33}
High rate	21^{+21}_{-11}	157^{+144}_{-66}	178^{+164}_{-75}

TABLE IV. Number of pairs of binary coalescence events with both SNRs between 15 and 30 and such that their mergers occur within 2 s or less from each other.

Run	BBH-BBH	BBH-BNS	BNS-BNS
Low rate	5	57	416
Median rate	11	304	6752
High rate	15	1594	41306

to each other, and on the low side, we focus on network SNRs roughly between 15 and 30. We consider overlapping events whose merger times either coincide (as a proxy for merger within the same second) or are separated by 2 s, again because these are the types of scenarios where biases will likely be the largest. The number of overlaps from the previous section that satisfy these criteria is given in Table IV, for different local merger rates; we see that they will be fairly common.

In our parameter estimation studies, for definiteness we take the BBH events to have masses similar to those of either GW150914 [75,76] (a higher-mass, shorter-duration signal) or GW151226 [57,76] (a lower-mass, longer-duration event), while for BNSs we take the masses to be similar to those of GW170817 [7,55]. Overlapping signals are given different injected sky locations. All analyses are done with three different noise realizations. For each example of overlapping signals, parameter estimation is also done on the individual signals, for the same noise realizations, in order to assess what biases occur. Figure 4 provides an overview of the various overlap scenarios that will be considered in the rest of this paper, in terms of masses and SNRs.

To reduce computational cost, we focus on nonspinning sources. A BBH signal is then characterized by parameters $\vec{\theta} = \{m_1, m_2, \alpha, \delta, \iota, \psi, D_L, t_c, \varphi_c\}$, where m_1 and m_2 are the component masses, (α, δ) specifies the sky position in terms of right ascension and declination, ι and ψ are, respectively, the inclination and polarization angles which specify the orientation of the orbital plane with respect to the line of sight, D_L is the luminosity distance, and t_c and φ_c are, respectively, the time and phase at coalescence. BNS signals have two additional parameters (Λ_1, Λ_2), corresponding to the (dimensionless) tidal deformabilities [77–81].

In this work, we focus specifically on potential biases in *intrinsic* parameters. For BBHs, results will be shown for the total mass $M = m_1 + m_2$ and mass ratio $q = m_2/m_1$ (with the convention $m_2 \leq m_1$). For BNSs, we show chirp mass $\mathcal{M}$ instead of total mass, since that parameter is usually the best-determined one for long signals. As the individual tidal deformabilities tend to be poorly measurable for the SNRs considered here, we will be showing results for a parameter $\tilde{\Lambda}$ defined as [82]

$$\tilde{\Lambda} = \frac{16}{13} \sum_{i=1,2} \Lambda_i \frac{m_i^4}{M^4} \left(12 - 11\frac{m_i}{M}\right), \quad (9)$$

since this is how tidal deformabilities enter the waveform phase to leading (5PN) order [77].

In the Bayesian framework, all information about the parameters of interest is encoded in the posterior *probability density function* (PDF), given by Bayes' theorem [83]:
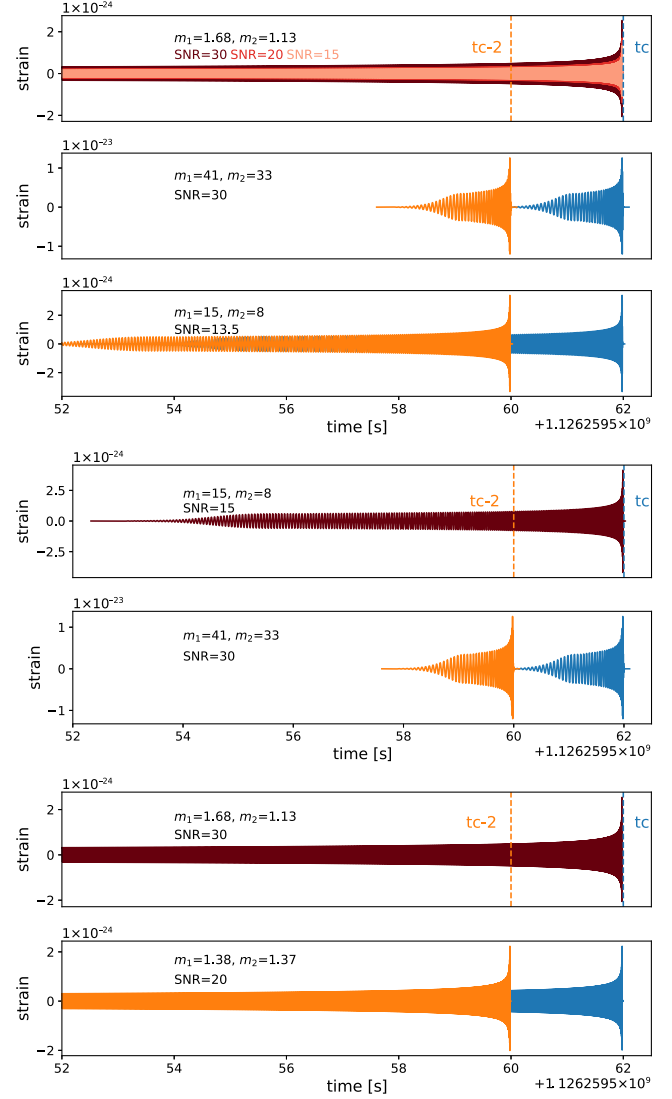

FIG. 4. Individual waveforms and the overlap scenarios considered in our simulations. All signals are injected in three different simulated noise realizations for a third-generation detector network. Signals are either overlapped using the same end time (blue waveforms) or 2 s earlier than the "primary" signal's end time (orange waveforms). Top three panels: BNS signals (top) with an SNR of 30, 20, or 15 being overlapped with either a high-mass BBH signal (middle; GW150914-like) or a low-mass BBH signal (bottom; GW151226-like). Middle panels: overlapping waveforms in the case of two BBH signals. The higher-mass BBH signal (bottom; GW150914-like) is overlapped with the lower-mass BBH signal (top; GW151226-like). Bottom panels: overlapping waveforms in the case of two BNS signals.

$$p(\vec{\theta}|\mathcal{H}_s, d) = \frac{p(d|\vec{\theta}, \mathcal{H}_s)p(\vec{\theta}|\mathcal{H}_s)}{p(d|\mathcal{H}_s)}, \quad (10)$$

where $\vec{\theta}$ is the set of parameter values and $\mathcal{H}_s$ is the hypothesis that a GW signal depending on the parameters $\vec{\theta}$ is present in the data d. For parameter estimation purposes,

the factor $p(d|\mathcal{H}_s)$, called the *evidence* for the hypothesis $\mathcal{H}_s$, is effectively set by the requirement that PDFs are normalized. Assuming the noise to be Gaussian, the *likelihood* $p(d|\vec{\theta}, \mathcal{H}_s)$ of obtaining data $d(t)$ given the presence of a signal $h(t)$ is determined by the proportionality

$$p(d|\vec{\theta}, \mathcal{H}_s) \propto \exp\left[-\frac{1}{2}(d - h(\vec{\theta})|d - h(\vec{\theta}))\right], \quad (11)$$

where the noise-weighted inner product $(\cdot|\cdot)$ is defined as

$$(a|b) = 4\text{Re} \int_{f_{\text{low}}}^{f_{\text{high}}} \frac{\tilde{a}^*(f)\tilde{b}(f)}{S_h(f)} df. \quad (12)$$

Here, a tilde refers to the Fourier transform, and $S_h(f)$ is the PSD, as in the previous section. Because of computational limitations, in our parameter estimation studies we use a lower-frequency cutoff of $f_{\text{low}} = 23$ Hz. Since both ET and CE will be sensitive down to lower frequencies than that, we expect that our choice will lead to conservative estimates of parameter estimation biases, as the same signal will, in reality, accumulate more SNR when it is visible in the detector already from a lower frequency.

Our choices for the *prior probability density* $p(\vec{\theta}|\mathcal{H}_s)$ in Eq. (10) are similar to what has been used for the analyses of real data when BBH or BNS signals were present with masses similar to the ones specified in Fig. 4. In all cases, we sample uniformly in component masses. For the GW150914-like signals, we do this in the range $m_1, m_2 \in [10, 80]$ $M_\odot$. For analyzing the GW151226-like signals, the component mass range is $m_1, m_2 \in [3, 54.4]$ $M_\odot$, and, in addition, we restrict chirp mass to $\mathcal{M} \in [5, 20]$ $M_\odot$ and mass ratio q to the range [0.05, 1]. For BNSs, we sample component masses in the range $m_1, m_2 \in [1, 2]$ $M_\odot$, restricting $\mathcal{M} \in [0.7, 2]$ $M_\odot$, while tidal deformabilities are sampled uniformly in the range $\Lambda_1, \Lambda_2 \in [0, 5000]$. When we show PDFs for the derived quantity $\tilde{\Lambda}$, they will have been reweighted with the prior probability distribution of this parameter induced by the flat priors on component masses and Λ_1 and Λ_2, such as to effectively have a uniform prior on $\tilde{\Lambda}$.

To sample the likelihood function in Eq. (11), we use the LALInference library [84] and, specifically, the lalinference_mcmc algorithm. The waveforms we use for the BNS and BBH signals are IMRPhenomD_NRTidalv2 [85–87] and IMRPhenomD [88,89] respectively, both computed with the waveform library LALsimulation. To inject the signals and add noise to them, we use standard tools available within the LALsimulation package. All these codes are openly accessible in LALsuite [90].

For our parameter estimation studies, signals are added to stationary, Gaussian noise following the projected ET and CE PSDs [26–29]. These are also the PSDs used in calculating the likelihood in Eq. (11). We note that, in reality, the PSD would be estimated from the data themselves, which is currently done either by characterizing the

noise in a segment of data adjacent to the one being analyzed [84] or through an algorithm such as BayesWave which simultaneously characterizes signal, Gaussian noise, and possible instrumental glitches [91–93]. However, the first method implicitly assumes the absence of signals in the "off-source" data segment, while at present the second one assumes the presence of a *single* signal in the "on-source" segment which is consistent with a particular sky location and orientation of the source. Hence, in a situation where multiple signals are present in almost any stretch of data, the PSD estimation is itself problematic. For now, we ignore this issue, but possible solutions will be discussed in Sec. V.

Before performing parameter estimation, we verify the detectability of the individual signals in the overlap scenarios in Fig. 4 using the PYCBC software package [94]. We inject overlapping signals in noise generated from the PSD and check that the individual signals show up as triggers with masses that are consistent between detectors, at a network SNR above a threshold of 8. This turns out to be true for all the cases considered, except for two BBH signals merging at the same time. In the latter case, we still have triggers in individual detectors but with masses differing by up to ~ 5 $M_\odot$. Using the SNRs in single detectors as detection statistics, detection is still achieved. For all scenarios, the end times of individual signals tend to be identified with a precision of a few milliseconds [95]; when subsequently performing parameter estimation, we use a prior range for end time that is centered on the true end time, leaving an interval of 0.1 s on either side.

All simulations are done with three different noise realizations. In the next section, results are shown for one of those; for the other two noise realizations, see the Appendix.

As usual, the one-dimensional PDF $p(\lambda|\mathcal{H}_s, d)$ for a particular parameter λ is obtained from the joint PDF $p(\vec{\theta}|\mathcal{H}_s, d)$ by integrating out all other parameters. In assessing the effect on parameter estimation of signals that overlap in various ways, we will frequently be comparing one-dimensional PDFs for the same parameter in different situations. A convenient way of quantifying the difference between two distributions $p_1(\lambda)$ and $p_2(\lambda)$ is by means of the *Kolmogorov-Smirnov (KS) statistic* [96,97]. Let $P_1(\lambda)$ and $P_2(\lambda)$ be the associated *cumulative* distributions; then the KS statistic is just the largest distance between these two:

$$\text{KS} = \sup_\lambda |P_1(\lambda) - P_2(\lambda)|. \quad (13)$$

By construction, this yields a number between 0 and 1; if the KS statistic is close to zero, then the distributions $p_1(\lambda)$ and $p_2(\lambda)$ will be considered close to each other. To establish a benchmark, one can look at differences in PDFs obtained through different sampling methods, e.g., LALInference versus BILBY, with typical KS statistics of a
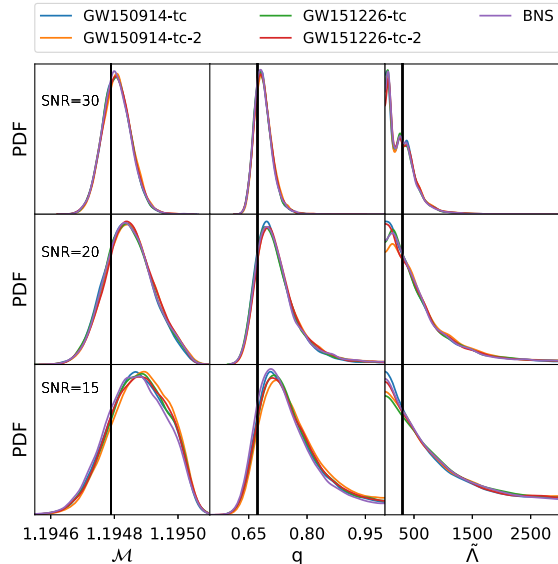
FIG. 5. Posterior PDFs showing estimation of intrinsic parameters when the BNS signal has SNR = 30 (top row), SNR = 20 (middle row), and SNR = 15 (bottom row). Results are shown for the cases when the GW150914-like signal ends at the same time as the BNS signal (GW150914-tc), when it ends 2 s earlier (GW150914-tc-2), when the GW151226-like signal ends at the same time as the BNS (GW151226-tc), when it ends 2 s earlier (GW151226-tc-2), and finally when the injected signal is only the BNS (BNS). The true values of the parameters are indicated by vertical black lines.

few percent [98] for the kinds of SNRs considered in the present paper. Hence, for our purposes we will take large biases in parameter estimation to mean KS values significantly higher than that, for the same noise realization. Finally, we note that in 3G detectors larger SNRs will be seen than those considered here, but exploring how biases scale with SNR would require a much larger study than our computational resources permit.

IV. RESULTS

A. Overlap of a BNS signal with a BBH signal

First, we look at the results of parameter estimation for the overlap of a BNS signal with a BBH, either ending at

the same time or with the BBH signal ending 2 s earlier than the BNS. This is the scenario shown in the top panels in Fig. 4. We perform parameter estimation first on the BNS and then on the BBH, with priors as specified in the previous section.

1. BNS recovery

Figure 5 shows posterior probability distributions for intrinsic parameters characterizing the BNS signal, for three different SNRs of the BNS, and the different overlap scenarios. The PDFs tend to widen with decreasing SNR, as expected. We see that estimation of the mass parameters is essentially unaffected, regardless of the type of overlapping BBH signal (GW150914-like or GW151226-like) or of its merger time (identical to that of the BNS or 2 s earlier). For a given SNR of the BNS, the PDFs for the tidal parameter $\tilde{\Lambda}$ differ slightly more between the overlap scenarios. However, we note that most of the information on tides enters the signal at high frequencies, where the detectors are less sensitive; and in fact, as shown in the Appendix (Fig. 9), differences in the underlying noise realization tend to have a larger effect on the measurement of $\tilde{\Lambda}$ than overlapping signals.

We conclude that an overlapping BBH signal does not have much impact on the estimation of the BNS parameters, even if the BBH merger time is arbitrarily close to that of the BNS. This is corroborated by the KS statistics in Table V, which compare PDFs for the various overlap scenarios with the corresponding PDFs in the absence of overlapping signals. It is reasonable to assume that placing a BBH signal even earlier in the BNS would also have had little impact.

2. BBH recovery

Figure 6 shows parameter estimation on the BBHs when the SNR of the BNS signal is varied from 30, to 20, to 15. Table VI has the corresponding KS statistics comparing with PDFs obtained in the absence of overlap. Again, results are shown for a particular noise realization; see Fig. 10 in the Appendix for two other noise realizations. We see that when the BBH signal has a time of coalescence 2 s earlier than the BNS (tc-2 in the figure) the signal is well

TABLE V. Values of the KS statistic comparing PDFs for BNS parameters (columns) in the BNS + BBH overlap scenarios (rows) with the corresponding PDFs when there is no overlapping BBH signal. The small numbers indicate the absence of significant bias. The numbers shown here correspond to the PDFs in Fig. 5.

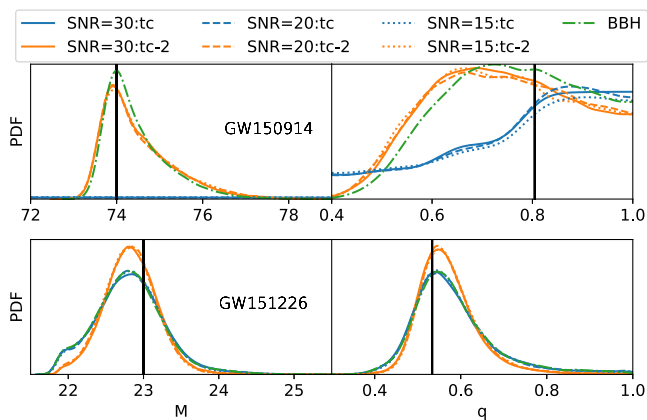| BBH overlapped	BNS (SNR = 30)			BNS (SNR = 20)			BNS (SNR = 15)		
	$\mathcal{M}$	q	$\tilde{\Lambda}$	$\mathcal{M}$	q	$\tilde{\Lambda}$	$\mathcal{M}$	q	$\tilde{\Lambda}$
GW150914-tc	0.0112	0.00915	0.0277	0.0162	0.0204	0.0275	0.0297	0.0323	0.00947
GW150914-tc-2	0.0320	0.0389	0.0168	0.0235	0.0273	0.0331	0.0704	0.0840	0.0218
GW151226-tc	0.00754	0.00748	0.0113	0.0123	0.0139	0.0173	0.0403	0.0516	0.0305
GW151226-tc-2	0.0187	0.0220	0.0309	0.0227	0.0233	0.0259	0.0521	0.0513	0.0159

FIG. 6. Posterior PDFs for the total mass and mass ratio, for the GW150914-like signal (top panel) and the GW151226-like signal (bottom panel) when they are, respectively, being overlapped with a BNS signal of SNR = 30 (solid lines), SNR = 20 (dashed lines), and SNR = 15 (dotted lines). The overlaps are being done when the BBH and the BNS end at the same time (tc) and when the BBH ends 2 s before the BNS (tc-2). Finally, posterior PDFs for the two BBH signals by themselves are shown as green, dash-dotted lines (BBH). The injected parameter values are indicated by black vertical lines.
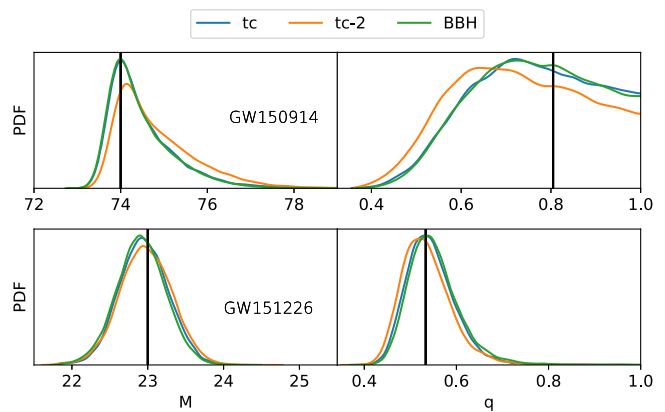
FIG. 7. Posterior PDFs for total mass and mass ratio when a GW150914-like signal and a GW151226-like signal are being overlapped at the same trigger times (tc) and when the trigger time of the GW150914-like BBH ends 2 s earlier (tc-2), compared with parameter estimation in the absence of overlap (BBH). The top panel shows the recovery of the GW150914-like signal and the bottom one that of the GW151226-like signal. Black vertical lines indicate the true values of the parameters.

recovered. However, when the BBH signal and the BNS signal end at the same instant of time, the BBH recovery deteriorates, and, in the case of the GW150914-like signal, the sampling process, in fact, fails to find the signal. For the GW151226-like signal, while the estimates are offset from their true values, there is some measurability of the signal when the times of coalescence of the BBH and BNS are the same. The different outcomes between the GW150914-like and GW151226-like injection are likely due to the short duration of the GW150914-like signal, effectively leading to a distortion of the entire signal when the merger happens at the same instant as the BNS merger. By contrast, the much longer inspiral of the GW151226-like signal implies many more wave cycles for the parameter estimation algorithm to latch onto. Finally, as the SNR over the underlying BNS signal is varied (keeping the SNR of the BBH signal the same), the PDFs for the BBH show essentially no change. Placing a BBH signal only 2 s

before the BNS merger causes the BBH to be recovered without appreciable biases, so it is reasonable to assume that placing a BBH signal still earlier in the BNS inspiral would also have little effect on its recovery.

B. Overlap of two BBH signals

The scenario being analyzed here is the one in the middle panels in Fig. 4. Figure 7 shows the posterior PDFs on total mass M and mass ratio q when two BBH signals of different masses are being overlapped, compared with parameter estimation on the same signals in situations where there is no overlap (BBH). The corresponding KS statistic values are given in Table VII. We find the results to be consistent within statistical fluctuations. Here, too, the signals are overlapped once with the same coalescence times (tc) and once with one of the signals, GW150914, ending 2 s earlier (tc-2). The SNRs of the two signals, GW150914-like, and GW151226-like, are 30 and 15, respectively. As can be seen in the figure, the two BBH signals' parameters can be extracted without any biases

TABLE VI. Values of the KS statistic comparing PDFs for BBH parameters (columns) in the BNS + BBH overlap scenarios (rows) with the corresponding PDFs when there is no overlapping BNS signal. In the case of a GW150914-like signal merging at the same time as a BNS, the sampler fails to find the signal, but other scenarios are not so problematic. For GW151226, the slightly higher values for the tc-2 case compared to the tc case are likely due to the signals being placed in a slightly different part of the noise stream (2 s earlier) from the BBH-only cases that are used for comparison. The numbers shown here correspond to the PDFs in Fig. 6.

BNS overlapped	GW150914-tc		GW150914-tc-2		GW151226-tc		GW151226-tc-2	
	M	q	M	q	M	q	M	q
BNS (SNR = 15)	⋯	⋯	0.0504	0.0807	0.00933	0.0117	0.0687	0.0657
BNS (SNR = 20)	⋯	⋯	0.0427	0.0698	0.0107	0.0106	0.0727	0.0700
BNS (SNR = 30)	⋯	⋯	0.0379	0.0673	0.0187	0.183	0.0819	0.0793

TABLE VII. Values of the KS statistic comparing PDFs for BBH parameters in the BBH + BBH overlap scenarios with the corresponding PDFs without an overlapping signal. The slightly higher values for the tc-2 cases are likely due to the signals being in a slightly different part of the noise stream (2 s earlier) from the BBH-only cases used for comparison. However, in all cases there is no significant bias. The numbers shown here correspond to the PDFs in Fig. 7.

GW150914-tc		GW150914-tc-2		GW151226-tc		GW151226-tc-2	
M	q	M	q	M	q	M	q
0.0195	0.0109	0.162	0.103	0.0446	0.0478	0.0844	0.127

even when they end simultaneously. Again, see the Appendix for other noise realizations, with the same conclusion.

C. Overlap of two BNS signals

Finally, we analyze the simulations in the bottom panels in Fig. 4. Figure 8 shows the recovery of BNS parameters for each BNS signal when two BNS signals are being overlapped, again with either the same coalescence times and when one of the BNSs (henceforth BNS2) ends 2 s earlier than the other BNS signal (henceforth BNS1). For KS statistic values comparing PDFs with the corresponding nonoverlapping cases, see Table VIII. BNS1 and BNS2, respectively, have SNRs of 30 and 20 and component masses $(m_1, m_2) = (1.68, 1.13) M_\odot$ and $(m_1, m_2) = (1.38, 1.37) M_\odot$. These particular choices cause both signals to have very similar chirp masses. Given these masses, their tidal deformabilities, $\tilde{\Lambda} = 303$ for BNS1 and $\tilde{\Lambda} = 292$ for BNS2, follow the equation of state APR4; these were the simulated signals used for investigating systematics in the measurements on GW170817 in Ref. [55].

In Fig. 8, the top panel shows the posterior PDFs on chirp mass, mass ratio, and tidal deformability for BNS1 when BNS2 ends at the same time (tc) and when BNS2 ends 2 s earlier (tc-2), together with the case where only BNS1 is present in the data (BNS). The bottom panels show the same but for the recovery of BNS2. When the two signals end at the same time, the parameters characterizing BNS1 are being recovered, which likely happens because of the higher SNR of BNS1. As the tidal deformabilities of
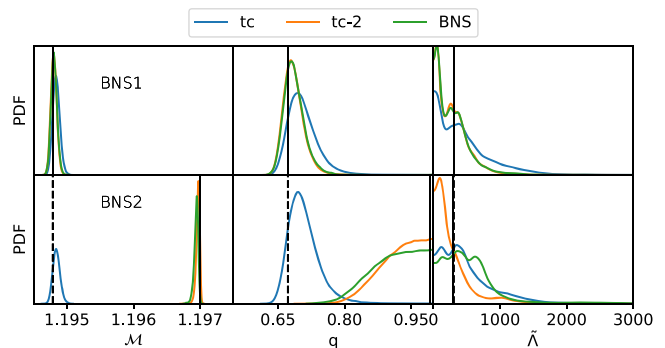

FIG. 8. Posterior PDFs showing recovery on chirp mass, mass ratio, and tidal deformability $\tilde{\Lambda}$ when two BNSs, referred to as BNS1 and BNS2, are being overlapped at the same time of coalescence (tc) and when BNS2 ends 2 s earlier than BNS1 (tc-2). These are compared with results in the absence of overlap (BNS). The top panel is for the recovery of BNS1 and the bottom one for the recovery of BNS2. The solid black vertical lines indicate the injected values of the source being recovered each time. We note that, when the times of coalescence of the two BNSs are the same, the parameter estimates recovered are those of BNS1, whose injected values are also shown in the bottom panel as dashed vertical black lines.

the two sources are so close, the PDFs for $\tilde{\Lambda}$ look similar in all cases. However, also looking at the mass parameters, parameter estimation is rather robust when the signals end 2 s apart.

V. CONCLUSIONS

Given regular improvements in the sensitivity of gravitational-wave detectors and especially the planned construction of the next generation of interferometers, it will become increasingly likely that individually detectable gravitational-wave signals will end up overlapping in the data. In this paper, we (i) assessed how often different types of overlap will happen in ET and CE and (ii) tried to quantify the impact this would have on parameter estimation with current data analysis techniques.

To address the question of the nature and frequency of different overlap scenarios, for each of three possible local merger rates, we constructed a catalog of signals in ET and CE, enabling a more in-depth study of overlaps than in previous works. We showed that there will be a significant

TABLE VIII. Values of the KS statistic comparing PDFs for BNS parameters in the BNS + BNS overlap scenarios with the corresponding PDFs without an overlapping signal; see also Fig. 8. We see that the numbers are higher for both BNSs when they end at the same time; in fact, the measured parameters for BNS2 are those of BNS1. However, when the BNSs merge 2 s apart, the values are much lower, showing that the biases largely disappear. The numbers shown here correspond to the PDFs in Fig. 8.

BNS1 (tc)			BNS1 (tc-2)			BNS2 (tc)			BNS2 (tc-2)		
$\mathcal{M}$	q	$\tilde{\Lambda}$	$\mathcal{M}$	q	$\tilde{\Lambda}$	$\mathcal{M}$	q	$\tilde{\Lambda}$	$\mathcal{M}$	q	$\tilde{\Lambda}$
0.269	0.270	0.202	0.0309	0.0216	0.0129	1.0	0.955	0.0762	0.384	0.0951	0.368

number of signals for which the merger happens within the same second, varying from tens to thousands depending on the local merger rate. Additionally, the substantial increase in the duration of BNS events due to the improved low-frequency sensitivity of third-generation observatories will lead to the occurrence of up to tens of other signals overlapping with a given BNS.

Motivated by these results, we performed the first detailed Bayesian analysis study on possible biases that may arise in future as detection rates become higher and overlapping signals start to occur. We focused on over-lapping signals for which the end times were close to each other, so that, in particular, there is overlap at times where both signal amplitudes are high; it is this type of situation where we expect parameter estimation biases to be the most pronounced. Specifically, merger times were taken to be either the same (as a proxy for being arbitrarily close to each other) or separated by 2 s. As a first proof-of-principle study, we have focused on a selected number of binary sources, and a generic statement about systematic errors from source overlap can be made only if a much larger number of sources are simulated for each overlap scenario. Our preliminary conclusions (based on a limited number of investigations) are as follows.

(i) When BBH signals are overlapping with a BNS signal of similar SNR, parameter estimation on the BNS is hardly affected, even with the merger time of the BBH arbitrarily close to that of the BNS. Presumably, this is due to the much larger number of BNS wave cycles in the band compared to the BBH.

(ii) However, in the same scenario, parameter estimation on the BBH lead to large offsets for underlying binary neutron star signals of SNRs lying between 15 and 30 and in three different noise realizations if the BBH is high mass, so that its signal is short. That said, the problem largely disappears when the BNS and BBH merger times are separated by 2 s or when the BBH is low mass.

(iii) When two BBHs with sufficiently dissimilar masses overlap with close-by merger times, parameter estimation on either of the signals will not be much affected.

(iv) When two BNS signals overlap with close-by merger times, parameter estimation will recover the louder signal reasonably well. With a 2 s separation of merger times, good-quality parameter estimation can already be done on the two signals separately.

These results suggest that current parameter estimation techniques will, in several types of situations of interest, already perform reasonably well in the 3G era when applied to overlapping signals, even when the individual signals have similar SNRs and even when the SNRs are on the low side given the projected distribution for these observatories. Nevertheless, a number of questions remain. What happens

when SNRs are gradually increased? Related to this is the choice of lower cutoff frequency; to what extent will parameter estimation improve as one goes to $f_{\text{low}} = 5$ Hz or even lower, so that signals have a much larger number of wave cycles in the detector's sensitive band? Though not the focus here, at higher SNRs, the use of currently available waveform approximants to analyze BNS signals in 3G detectors would lead to biases in the estimation of $\tilde{\Lambda}$ even in the absence of overlap [99], also motivating further research in waveform modeling. Spins were not included in our study, but it would be of interest to see their effect: Large precessing spins will complicate parameter estimation in the case of BBHs, while, for BNSs, having access to the spin-induced quadrupole moment can aid in determining tidal deformabilities [100]. Finally, what happens when overlaps involve (much) more than two signals, e.g., a long BNS signal overlapping with a large number of BBH signals? These questions are left for future work.

In order to make optimal scientific use of the capabilities of 3G detectors, it will be appropriate to develop Bayesian parameter estimation techniques for which the likelihood function assumes multiple signals to be present in a given stretch of data, e.g., replacing Eq. (11) by

$$p(d|\{\vec{\theta}_i\}, \mathcal{H}_s) \propto \exp\left[-\frac{1}{2}\left(d - \sum_{i=1}^{N} h(\vec{\theta}_i)\bigg| d - \sum_{i=1}^{N} h(\vec{\theta}_i)\right)\right],$$

(14)

with N the number of signals found by a detection pipeline and $\vec{\theta}_i$, $i = 1, ..., N$, the associated parameters. Additionally, one could let N itself be a parameter to be sampled over, thus allowing for an *a priori* unknown number of signals in the given stretch of data.

Another problem that will need to be addressed at the same time is that of measuring the PSD, which enters expressions for the likelihood through the inner product in, e.g., Eq. (14) above. Currently, PSD estimation is performed either by (i) computing the PSD from a stretch of data adjacent to the one being analyzed [84] or (ii) by simultaneously characterizing signal, Gaussian noise, and instrumental glitches [91–93]. However, the first method implicitly assumes the absence of signals in the "off-source" data segment. On the other hand, at least in the case of the triangular ET, the data from the three detectors can be added together to form a *null stream* [68], which by construction removes all signals present; if correlations between detectors can be neglected, then this enables the estimation of an average PSD over detectors [48]. However, this technique does not extend to, e.g., an ET-CE network even when only one signal is present in the data, unless the sky position is known. Regarding the second method, at present, it models a signal as a feature in the data that has

coherent power in multiple detectors in a way that is consistent with one specific sky location and orientation of the source (neither of which needs to be known *a priori*), but it may be feasible to extend this framework to a situation where one can expect there to be multiple relevant sky locations and source orientations corresponding to multiple signals.

In all this, it may be possible to borrow from techniques developed in the context of somewhat related problems in GW data analysis, such as the characterization of the large number of (in this case, near-monochromatic) signals from galactic white dwarf binaries in the space-based Laser Interferometer Space Antenna [101–107], BNSs in Big Bang Observer [43], or supermassive black hole binaries in pulsar timing searches [108].

APPENDIX: PARAMETER ESTIMATION FOR DIFFERENT NOISE REALIZATIONS

We have performed all our simulations in three different noise realizations. To avoid plots getting too busy, in Sec. IV, we showed results for only one of these; here, we also give them for the other two noise realizations.

In the case of a BNS overlapping with a BBH, the measurements on the BNS are shown in Fig. 9 and those on the BBH in Fig. 10. The corresponding KS values are given in Tables IX and X, respectively. For measurements on the mass parameters of the BNS, we find that the results are consistent between noise realizations. For the tidal parameter $\tilde{\Lambda}$, the PDFs differ somewhat more; compare the right columns in the two panels in Fig. 9. This is likely because most of the information on tides enters the signal at higher frequencies, where the variance of the noise is larger; hence, the measurement of $\tilde{\Lambda}$ will be more affected by the noise realization than the mass measurements, especially when SNRs are not high. Indeed, though not shown here explicitly, KS statistics for $\tilde{\Lambda}$ between different noise realizations, but for the same overlap situation, tend to be significantly larger than within the same noise realization but for different overlaps. For parameter estimation on the BBH, there are differences in the PDFs for the masses
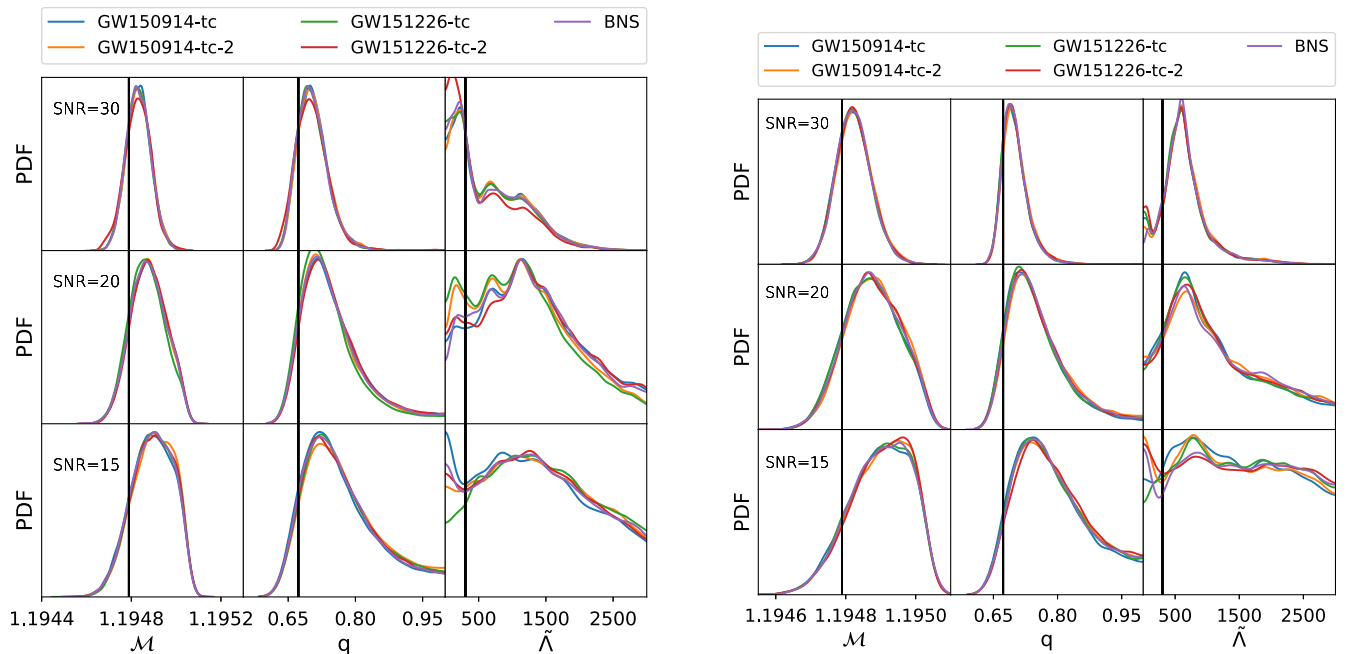

FIG. 9.   Posterior PDFs for BNS parameters when a BNS and BBH signal are being overlapped; the same as Fig. 5 when injections are done in two other noise realizations (left and right panels).
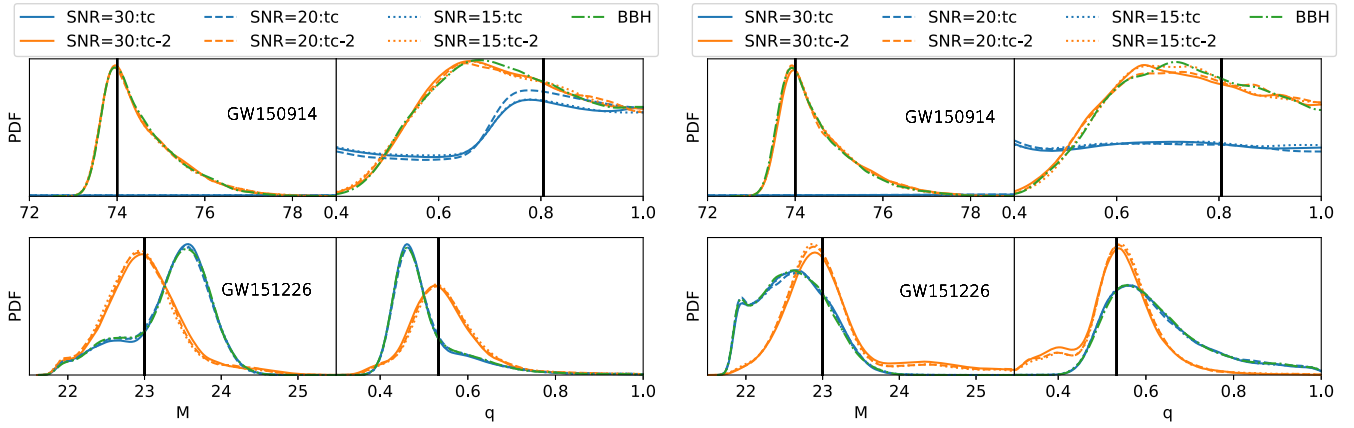
FIG. 10. Posterior PDFs for BBH parameters when a BNS and BBH signal are being overlapped; the same as Fig. 6 when injections are done in two other noise realizations.

TABLE IX. Values of the KS statistic comparing PDFs for BNS parameters (columns) in the BNS + BBH overlap scenarios (rows) with the corresponding PDFs when there is no overlapping BBH signal, when injections are done in two other noise realizations. The numbers shown correspond to the PDFs in Fig. 9, noise realization 2 corresponding to the left panel and noise realization 3 to the right panel.

BBH overlapped	BNS (SNR = 30)			BNS (SNR = 20)			BNS (SNR = 15)		
Noise realization 2	$\mathcal{M}$	q	$\tilde{\Lambda}$	$\mathcal{M}$	q	$\tilde{\Lambda}$	$\mathcal{M}$	q	$\tilde{\Lambda}$
GW150914-tc	0.0267	0.0248	0.0224	0.0106	0.0141	0.0169	0.0146	0.0211	0.0290
GW150914-tc-2	0.0287	0.0282	0.0338	0.00601	0.0108	0.0486	0.0263	0.0308	0.0137
GW151226-tc	0.0125	0.0141	0.0421	0.0376	0.0471	0.0723	0.0155	0.0152	0.0333
GW151226-tc-2	0.0337	0.0346	0.0815	0.0244	0.0258	0.0179	0.0113	0.0108	0.00923
Noise realization 3	$\mathcal{M}$	q	$\tilde{\Lambda}$	$\mathcal{M}$	q	$\tilde{\Lambda}$	$\mathcal{M}$	q	$\tilde{\Lambda}$
GW150914-tc	0.0140	0.0143	0.0251	0.0236	0.0298	0.0481	0.0114	0.0255	0.0378
GW150914-tc-2	0.0296	0.0396	0.0255	0.0272	0.0218	0.0125	0.0186	0.0125	0.0299
GW151226-tc	0.0135	0.0161	0.0347	0.0215	0.0312	0.0412	0.00750	0.00868	0.0239
GW151226-tc-2	0.0142	0.0140	0.0334	0.0109	0.00833	0.0310	0.0223	0.0292	0.0169

TABLE X. Values of the KS statistic comparing PDFs for BBH parameters (columns) in the BNS + BBH overlap scenarios (rows) with the corresponding PDFs when there is no overlapping BNS signal, when injections are done in two other noise realizations. As before, when the GW150914-like signal ends at the same time as a BNS, it is not found by the sampling algorithm, but other scenarios are less problematic. The numbers shown correspond to the PDFs in Fig. 10, noise realization 2 corresponding to the left panel and noise realization 3 to the right panel.

| BNS overlapped	GW150914-tc		GW150914-tc-2		GW151226-tc		GW151226-tc-2	
Noise realization 2	M	q	M	q	M	q	M	q
BNS (SNR = 15)	$\cdots$	$\cdots$	0.0134	0.011	0.00832	0.00890	0.411	0.398
BNS (SNR = 20)	$\cdots$	$\cdots$	0.0104	0.0109	0.0169	0.0172	0.390	0.377
BNS (SNR = 30)	$\cdots$	$\cdots$	0.0100	0.0113	0.0140	0.0146	0.367	0.357
Noise realization 3	M	q	M	q	M	q	M	q
BNS (SNR = 15)	$\cdots$	$\cdots$	0.0168	0.0100	0.0140	0.0142	0.318	0.131
BNS (SNR = 20)	$\cdots$	$\cdots$	0.0189	0.0131	0.0132	0.0137	0.322	0.315
BNS (SNR = 30)	$\cdots$	$\cdots$	0.0287	0.295	0.0136	0.0130	0.334	0.327
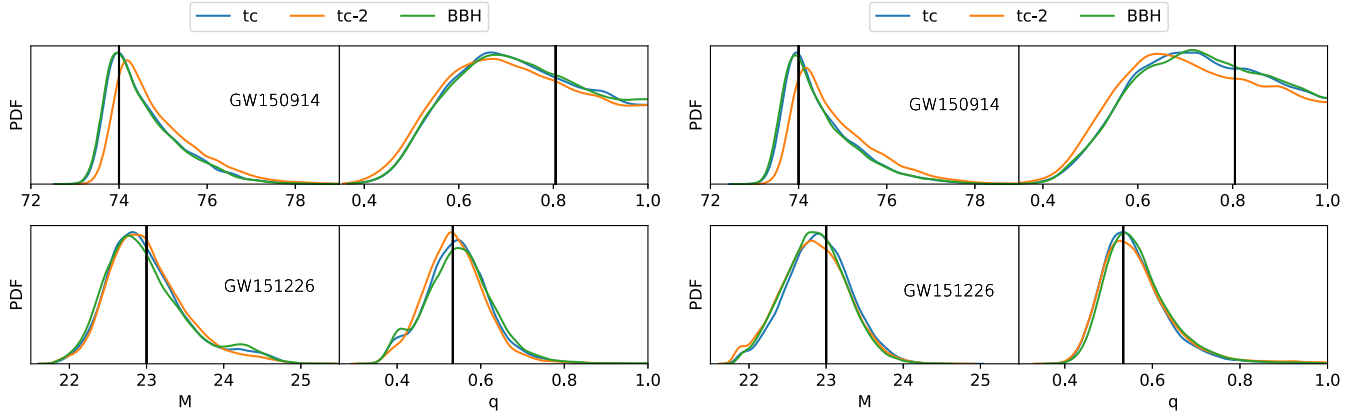
FIG. 11.   Posterior PDFs for BBH parameters when two BBH signals are being overlapped; the same as Fig. 7 when injections are done in two other noise realizations.

TABLE XI.   Values of the KS statistic comparing PDFs for BBH parameters in the BBH + BBH overlap scenarios with the corresponding PDFs for the BBH-only case, when injections are done in two other noise realizations. The numbers shown correspond to the PDFs in Fig. 11, the upper row corresponding to the left panel and the lower row to the right panel.

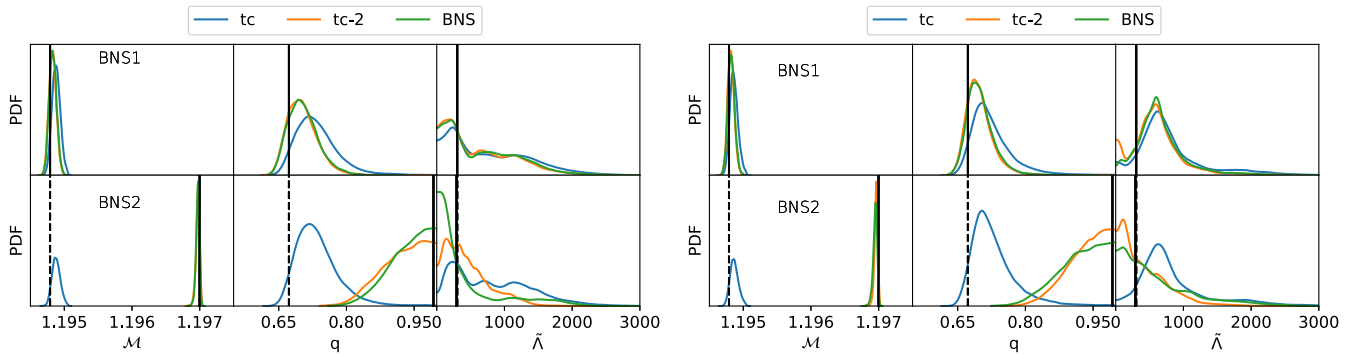| GW150914-tc		GW150914-tc-2		GW151226-tc		GW151226-tc-2	
M	q	M	q	M	q	M	q
0.0195	0.00854	0.163	0.0395	0.0299	0.0309	0.0417	0.0746
M	q	M	q	M	q	M	q
0.0291	0.0110	0.188	0.0625	0.0477	0.0497	0.0225	0.0440

FIG. 12.   Posterior PDFs when two BNS signals are being overlapped; the same as Fig. 8 when injections are done in two other noise realizations.

TABLE XII.   Values of the KS statistic comparing PDFs for BNS parameters in the BNS + BNS overlap scenarios with the corresponding PDFs for the BNS-only case, when injections are done in two other noise realizations. The numbers shown correspond to the PDFs in Fig. 12, the upper row corresponding to the left panel and the lower row to the right panel.

BNS1 (tc)			BNS1 (tc-2)			BNS2 (tc)			BNS2 (tc-2)		
$\mathcal{M}$	q	$\tilde{\Lambda}$	$\mathcal{M}$	q	$\tilde{\Lambda}$	$\mathcal{M}$	q	$\tilde{\Lambda}$	$\mathcal{M}$	q	$\tilde{\Lambda}$
0.316	0.282	0.0743	0.0385	0.0339	0.0325	1.0	0.936	0.382	0.0271	0.0858	0.248
$\mathcal{M}$	q	$\tilde{\Lambda}$	$\mathcal{M}$	q	$\tilde{\Lambda}$	$\mathcal{M}$	q	$\tilde{\Lambda}$	$\mathcal{M}$	q	$\tilde{\Lambda}$
0.278	0.257	0.123	0.0475	0.0381	0.0630	1.0	0.902	0.341	0.226	0.101	0.128

when the BBH merger time coincides with that of the BNS, but not so much if it occurs 2 s earlier.

In the case of two overlapping BBH signals, parameter estimation results are shown in Fig. 11 and KS statistics in Table XI. The results are quite robust under a change of noise realization.

Finally, the case of two overlapping BNSs with different noise realizations is shown in Fig. 12 and KS statistics in Table XII. As in the case of a BNS overlapping with a BBH, the PDFs for the masses are not much affected by differences in noise, but the ones for $\tilde{\Lambda}$ are more susceptible.

[1] B. Abbott *et al.* (LIGO Scientific and Virgo Collaborations), Astrophys. J. Lett. **818,** L22 (2016).

[2] B. P. Abbott *et al.* (LIGO Scientific and Virgo Collaborations), Phys. Rev. Lett. **116,** 221101 (2016); **121,** 129902 (E) (2018).

[3] B. P. Abbott *et al.* (LIGO Scientific and Virgo Collaborations), Astrophys. J. Lett. **882,** L24 (2019).

[4] B. P. Abbott *et al.* (LIGO Scientific and Virgo Collaborations), Phys. Rev. Lett. **123,** 011102 (2019).

[5] B. P. Abbott *et al.* (LIGO Scientific and Virgo Collaborations), Phys. Rev. D **100,** 104036 (2019).

[6] B. P. Abbott *et al.* (LIGO Scientific and Virgo Collaborations), Astrophys. J. Lett. **833,** L1 (2016).

[7] B. P. Abbott *et al.* (LIGO Scientific and Virgo Collaborations), Phys. Rev. X **9,** 031040 (2019).

[8] R. Abbott *et al.* (LIGO Scientific and Virgo Collaborations), Phys. Rev. X **11,** 021053 (2021).

[9] B. P. Abbott *et al.* (Virgo and LIGO Scientific Collaborations), Phys. Rev. Lett. **119,** 161101 (2017).

[10] B. Abbott *et al.* (LIGO Scientific and Virgo Collaborations), Phys. Rev. Lett. **121,** 161101 (2018).

[11] B. P. Abbott *et al.* (LIGO Scientific and Virgo Collaborations), Astrophys. J. Lett. **892,** L3 (2020).

[12] R. Abbott *et al.* (LIGO Scientific and Virgo Collaborations), Phys. Rev. D **102,** 043015 (2020).

[13] R. Abbott *et al.* (LIGO Scientific and Virgo Collaborations), Astrophys. J. Lett. **896,** L44 (2020).

[14] R. Abbott *et al.* (LIGO Scientific and Virgo Collaborations), Phys. Rev. Lett. **125,** 101102 (2020).

[15] R. Abbott *et al.* (LIGO Scientific and Virgo Collaborations), Astrophys. J. Lett. **900,** L13 (2020).

[16] B. P. Abbott *et al.* (LIGO Scientific, VINROUGE, Las Cumbres Observatory, DLT40, Virgo, 1M2H and MASTER Collaborations), Nature (London) **551,** 85 (2017).

[17] M. Soares-Santos *et al.* (DES, LIGO Scientific and Virgo Collaborations), Astrophys. J. Lett. **876,** L7 (2019).

[18] A. Palmese *et al.* (DES Collaboration), Astrophys. J. Lett. **900,** L33 (2020).

[19] M. Soares-Santos *et al.* (DES and Dark Energy Camera GW-EM Collaborations), Astrophys. J. Lett. **848,** L16 (2017).

[20] P. S. Cowperthwaite *et al.*, Astrophys. J. Lett. **848,** L17 (2017).

[21] B. P. Abbott *et al.* (LIGO Scientific, Virgo, Fermi-GBM and INTEGRAL Collaborations), Astrophys. J. **848,** L13 (2017).

[22] A. Albert *et al.* (ANTARES, IceCube, Pierre Auger, LIGO Scientific and Virgo Collaborations), Astrophys. J. Lett. **850,** L35 (2017).

[23] J. Aasi *et al.* (LIGO Scientific Collaboration), Classical Quantum Gravity **32,** 074001 (2015).

[24] F. Acernese *et al.* (VIRGO Collaboration), Classical Quantum Gravity **32,** 024001 (2015).

[25] https://gracedb.ligo.org/superevents/public/O3/.

[26] M. Punturo *et al.*, Classical Quantum Gravity **27,** 194002 (2010).

[27] S. Hild *et al.*, Classical Quantum Gravity **28,** 094013 (2011).

[28] D. Reitze *et al.*, Bull. Am. Astron. Soc. **51,** 035 (2019).

[29] B. P. Abbott *et al.*, Classical Quantum Gravity **34,** 044001 (2017).

[30] T. Regimbau, M. Evans, N. Christensen, E. Katsavounidis, B. Sathyaprakash, and S. Vitale, Phys. Rev. Lett. **118,** 151105 (2017).

[31] B. Sathyaprakash *et al.*, Classical Quantum Gravity **29,** 124013 (2012); **30,** 079501(E) (2013).

[32] T. Regimbau and S. A. Hughes, Phys. Rev. D **79,** 062002 (2009).

[33] B. S. Sathyaprakash, B. F. Schutz, and C. Van Den Broeck, Classical Quantum Gravity **27,** 215006 (2010).

[34] C. Van Den Broeck, in *Proceedings of the 12th Marcel Grossmann Meeting on General Relativity* (2010), pp. 1682–1685.

[35] W. Zhao, C. Van Den Broeck, D. Baskaran, and T. G. F. Li, Phys. Rev. D **83,** 023005 (2011).

[36] M. Punturo *et al.*, Classical Quantum Gravity **27,** 084007 (2010).

[37] B. Sathyaprakash *et al.*, in *Proceedings of the 46th Rencontres de Moriond on Gravitational Waves and Experimental Gravity* (2011), pp. 127–136.

[38] C. Van Den Broeck, J. Phys. Conf. Ser. **484,** 012008 (2014).

[39] M. Maggiore *et al.*, J. Cosmol. Astropart. Phys. 03 (2020) 050.

[40] B. S. Sathyaprakash *et al.*, arXiv:1903.09221.

[41] S. Vitale, W. M. Farr, K. K. Y. Ng, and C. L. Rodriguez, Astrophys. J. **886,** L1 (2019).

[42] K. K. Y. Ng, S. Vitale, W. M. Farr, and C. L. Rodriguez, Astrophys. J. Lett. **913,** L5 (2021).

[43] C. Cutler and J. Harms, Phys. Rev. D **73,** 042001 (2006).

[44] J. Harms, C. Mahrdt, M. Otto, and M. Prieß, Phys. Rev. D **77,** 123010 (2008).

[45] S. Sachdev, T. Regimbau, and B. Sathyaprakash, Phys. Rev. D **102**, 024051 (2020).

[46] A. Sharma and J. Harms, Phys. Rev. D **102**, 063009 (2020).

[47] S. Biscoveanu, C. Talbot, E. Thrane, and R. Smith, Phys. Rev. Lett. **125**, 241101 (2020).

[48] T. Regimbau *et al.*, Phys. Rev. D **86**, 122001 (2012).

[49] D. Meacher, K. Cannon, C. Hanna, T. Regimbau, and B. Sathyaprakash, Phys. Rev. D **93**, 024018 (2016).

[50] P. Relton and V. Raymond, arXiv:2103.16225.

[51] A. Antonelli, O. Burke, and J. R. Gair, arXiv:2104.01897.

[52] S. Vitale, Phys. Rev. D **94**, 121501 (2016).

[53] S. Vitale and M. Evans, Phys. Rev. D **95**, 064052 (2017).

[54] S. Vitale and C. Whittle, Phys. Rev. D **98**, 024029 (2018).

[55] B. P. Abbott *et al.* (LIGO Scientific and Virgo Collaborations), Phys. Rev. X **9**, 011001 (2019).

[56] B. Abbott *et al.* (LIGO Scientific and Virgo Collaborations), Phys. Rev. Lett. **116**, 061102 (2016).

[57] B. P. Abbott *et al.* (LIGO Scientific and Virgo Collaborations), Phys. Rev. Lett. **116**, 241103 (2016).

[58] B.-M. Hoang, S. Naoz, and K. Kremer, Astrophys. J. **903**, 8 (2020).

[59] M. Safarzadeh, E. Berger, K. K.-Y. Ng, H.-Y. Chen, S. Vitale, C. Whittle, and E. Scannapieco, Astrophys. J. Lett. **878**, L13 (2019).

[60] K. Belczynski, T. Ryu, R. Perna, E. Berti, T. Tanaka, and T. Bulik, Mon. Not. R. Astron. Soc. **471**, 4702 (2017).

[61] M. Oguri, Mon. Not. R. Astron. Soc. **480**, 3842 (2018).

[62] R. Abbott *et al.* (LIGO Scientific and Virgo Collaborations), Astrophys. J. Lett. **913**, L7 (2021).

[63] P. Ade *et al.* (Planck Collaboration), Astron. Astrophys. **571**, A16 (2014).

[64] T. P. Robitaille, E. J. Tollerud, P. Greenfield, M. Droettboom, E. Bray, T. Aldcroft, M. Davis, A. Ginsburg, A. M. Price-Whelan *et al.*, Astron. Astrophys. **558**, A33 (2013).

[65] A. M. Price-Whelan, D. W. Hogg, H.-W. Rix, N. De Lee, S. R. Majewski, D. L. Nidever, N. Troup, J. G. Fernández-Trincado, D. A. García-Hernández *et al.* (The Astropy Collaboration), Astron. J. **156**, 123 (2018).

[66] B. S. Sathyaprakash and S. V. Dhurandhar, Phys. Rev. D **44**, 3819 (1991).

[67] S. Kastha, M. Saleem, and K. Arun, Mon. Not. R. Astron. Soc. **496**, 523 (2020).

[68] A. Freise, S. Chelkowski, S. Hild, W. Del Pozzo, A. Perreca, and A. Vecchio, Classical Quantum Gravity **26**, 085012 (2009).

[69] S. Hild *et al.*, Classical Quantum Gravity **28**, 094013 (2011).

[70] S. Hild, S. Chelkowski, A. Freise, J. Franc, N. Morgado, R. Flaminio, and R. DeSalvo, Classical Quantum Gravity **27**, 015003 (2010).

[71] B. S. Sathyaprakash, E. Belgacem, D. Bertacca, C. Caprini, G. Cusin, Y. Dirian, X. Fan, D. Figueroa, S. Foffa, E. Hall, J. Harms, M. Maggiore, V. Mandic, A. Matas, T. Regimbau, M. Sakellariadou, N. Tamanini, and E. Thrane, arXiv:1903.09260.

[72] B. F. Schutz, Classical Quantum Gravity **28**, 125023 (2011).

[73] B. P. Abbott *et al.* (VIRGO, KAGRA and LIGO Scientific Collaborations), Living Rev. Relativity **21**, 3 (2018); **19**, 1 (2016).

[74] R. X. Adhikari, K. Arai, A. F. Brooks, C. Wipf, O. Aguiar, P. Altin, B. Barr, L. Barsotti, R. Bassiri, A. Bell *et al.*, Classical Quantum Gravity **37**, 165003 (2020).

[75] B. P. Abbott *et al.* (LIGO Scientific and Virgo Collaborations), Phys. Rev. Lett. **116**, 241102 (2016).

[76] B. P. Abbott *et al.* (LIGO Scientific and Virgo Collaborations), Phys. Rev. X **6**, 041015 (2016); **8**, 039903(E) (2018).

[77] E. E. Flanagan and T. Hinderer, Phys. Rev. D **77**, 021502 (2008).

[78] J. Vines, E. E. Flanagan, and T. Hinderer, Phys. Rev. D **83**, 084051 (2011).

[79] T. Damour, A. Nagar, and L. Villain, Phys. Rev. D **85**, 123007 (2012).

[80] W. Del Pozzo, T. G. F. Li, M. Agathos, C. Van Den Broeck, and S. Vitale, Phys. Rev. Lett. **111**, 071101 (2013).

[81] M. Agathos, J. Meidam, W. Del Pozzo, T. G. F. Li, M. Tompitak, J. Veitch, S. Vitale, and C. Van Den Broeck, Phys. Rev. D **92**, 023012 (2015).

[82] L. Wade, J. D. E. Creighton, E. Ochsner, B. D. Lackey, B. F. Farr, T. B. Littenberg, and V. Raymond, Phys. Rev. D **89**, 103012 (2014).

[83] J. Veitch and A. Vecchio, Phys. Rev. D **81**, 062003 (2010).

[84] J. Veitch *et al.*, Phys. Rev. D **91**, 042003 (2015).

[85] T. Dietrich, S. Bernuzzi, and W. Tichy, Phys. Rev. D **96**, 121501 (2017).

[86] T. Dietrich *et al.*, Phys. Rev. D **99**, 024029 (2019).

[87] T. Dietrich, A. Samajdar, S. Khan, N. K. Johnson-McDaniel, R. Dudi, and W. Tichy, Phys. Rev. D **100**, 044003 (2019).

[88] S. Husa, S. Khan, M. Hannam, M. Pürrer, F. Ohme, X. J. Forteza, and A. Bohé, Phys. Rev. D **93**, 044006 (2016).

[89] S. Khan, S. Husa, M. Hannam, F. Ohme, M. Pürrer, X. J. Forteza, and A. Bohé, Phys. Rev. D **93**, 044007 (2016).

[90] LIGO Scientific Collaboration, LIGO Algorithm Library—LALSuite, free software (GPL) (2018).

[91] N. J. Cornish and T. B. Littenberg, Classical Quantum Gravity **32**, 135012 (2015).

[92] B. Bécsy, P. Raffai, N. J. Cornish, R. Essick, J. Kanner, E. Katsavounidis, T. B. Littenberg, M. Millhouse, and S. Vitale, Astrophys. J. **839**, 15 (2017).

[93] N. J. Cornish, T. B. Littenberg, B. Bécsy, K. Chatziioannou, J. A. Clark, S. Ghonge, and M. Millhouse, Phys. Rev. D **103**, 044006 (2021).

[94] C. Biwer, C. D. Capano, S. De, M. Cabero, D. A. Brown, A. H. Nitz, and V. Raymond, Publ. Astron. Soc. Pac. **131**, 024503 (2019).

[95] C. Van Den Broeck and A. S. Sengupta, Classical Quantum Gravity **24**, 1089 (2007).

[96] A. N. Kolmogorov, Giornale dell'Istituto Italiano degli Attuari **4**, 83 (1933).

[97] N. Smirnov, Ann. Math. Stat. **19**, 279 (1948).

[98] I. M. Romero-Shaw *et al.*, Mon. Not. R. Astron. Soc. **499**, 3295 (2020).

[99] A. Samajdar and T. Dietrich, Phys. Rev. D **98**, 124030 (2018).

[100] A. Samajdar and T. Dietrich, Phys. Rev. D **100**, 024046 (2019).

[101] J. Crowder and N. J. Cornish, Phys. Rev. D **70**, 082004 (2004).

[102] N. J. Cornish and J. Crowder, Phys. Rev. D **72**, 043005 (2005).

[103] N. J. Cornish and E. K. Porter, Classical Quantum Gravity **24**, 5729 (2007).

[104] J. Crowder and N. Cornish, Phys. Rev. D **75**, 043008 (2007).

[105] T. B. Littenberg, Phys. Rev. D **84**, 063009 (2011).

[106] T. Robson and N. Cornish, Classical Quantum Gravity **34**, 244002 (2017).

[107] T. Littenberg, N. Cornish, K. Lackeos, and T. Robson, Phys. Rev. D **101**, 123021 (2020).

[108] A. Petiteau, S. Babak, A. Sesana, and M. de Araújo, Phys. Rev. D **87**, 064036 (2013).

[109] E. Pizzati, S. Sachdev, A. Gupta, and B. Sathyaprakash, arXiv:2102.07692.